Aerosol Science and Technology, 42:958–969, 2008

ISSN: 0278-6826 print / 1521-7388 online
DOI: 10.1080/02786820802363827

Albedo Measurements and Optical Sizing of Single Aerosol Particles

Todd J. Sanford,[1,2] Daniel M. Murphy,[1] David S. Thomson[1,2,*] and Richard W. Fox[3]

[1]*NOAA Earth System Research Laboratory, Boulder, Colorado, USA*
[2]*Cooperative Institute for Research in the Environmental Sciences, University of Colorado, Boulder, Colorado, USA*
[3]*National Institute of Standards and Technology, Boulder, Colorado, USA*

Aerosols play an important role in global climate change by their interactions with incoming solar radiation and outgoing longwave radiation from the planetary surface. The climate effects of aerosols depend on their scattering and absorption properties. This article describes the development of an instrument (ASTER: Aerosol Scattering To Extinction Ratio) that simultaneously measures the scattering and extinction of single aerosol particles. ASTER uses a high-Q cavity to amplify the extinction signal and innovative optics to collect the scattered light. It can distinguish many partially absorbing particles from a few black ones even if the bulk absorption is the same. Optical sizing and single-scattering albedo measurements were made for laboratory-generated particles with diameters from about 300 nanometers to above one micrometer. Using this prototype instrument, changes in albedo for single particles of 20% or greater were detected by measurement of the scattering and extinction. Optical sizing of the individual particles to within ~50 nm was accomplished using the ratio of the forward scattered light to the total scattering. Initial measurements of laboratory air showed a mode of highly absorbing particles. This article reports design and early laboratory tests on ASTER.

INTRODUCTION

Aerosol particles in the atmosphere are known to play critical roles in the global climate system by affecting the radiative balance of the Earth system (IPCC 2007). Aerosols contribute to radiative forcing by the absorption and scattering of incoming solar radiation and outgoing thermal radiation from the Earth's surface (Chylek and Coakley 1974). An important quantity in the description of aerosol absorption and scattering is the single-scattering albedo (SSA), ω_0. The extinction coefficient, σ_{ep}, is the sum of the scattering coefficient, σ_{sp}, and the absorption coefficient, σ_{ap}. In terms of these coefficients, $\omega_0 = \sigma_{sp}/\sigma_{ep}$ and gives the fraction of extinction that is due to scattering. Aerosols with $\omega_0 = 1$ are pure scatterers and those with $\omega_0 < 1$ have an absorption component. Depending on the reflectivity of the underlying surfaces, it has been suggested that aerosols with $\omega_0 < 0.85$ produce a net warming effect to the climate system and those with values greater than this yield a net cooling effect (Penner 2001).

Much of the light absorption in atmospheric aerosols is due to black carbon (Bond and Bergstrom 2005), minerals such as hematite (Buseck and Posfai 1999; Lafon et al. 2006) and probably other absorbing organic material (Andreae and Gelencser 2006). The sources of black carbon are largely incomplete combustion emissions and biomass burning. A key factor in the absorption coefficient and thus in SSA is the mixing state of the black carbon in aerosols (Ackerman and Toon 1981; Fuller et al. 1999; Jacobson 2001). Black carbon in the atmosphere that is found in a mixture with other chemical species, such as a black carbon core surrounded with a coating, is termed internally mixed black carbon. Numerous studies have demonstrated that elemental carbon is quite prevalent in the atmosphere with tiny inclusions in as many as 90% of the submicrometer particles in the polluted North Atlantic (Buseck and Posfai 1999). Even in cleaner environments in the lower to mid-troposphere percentages of elemental carbon containing particles were found to be in the 10–50% range (Posfai et al. 1999; Buseck and Posfai 1999). Recent work has also determined that a few percent of the aerosol particles in the upper troposphere-lower stratosphere region contain black carbon with approximately 40% of all black carbon measured showing evidence of internal mixing (Schwarz et al. 2006).

Understanding the sources and atmospheric processing of light-absorbing particles necessitates an in-situ, single-particle instrument for the measurement of the optical properties of various classes of absorbing aerosols, including black carbon. Numerous methods have been employed for the measurement of scattering and absorption (or extinction) coefficients of aerosols.

Received 3 March 2008; accepted 31 July 2008.

*Now at Droplet Measurement Technologies, Boulder, CO USA.

The authors wish to acknowledge funding from NOAA and NASA climate research. Dr. Erik Richard is also gratefully acknowledged for work in the initial phases of the instrument development.

Address correspondence to Todd Sanford, NOAA Earth System Research Laboratory, 325 Broadway CSD2, Boulder, CO 80305-3337, USA. E-mail: todd.j.sanford@noaa.gov

A widely used method for aerosol absorption measurements has been the collection of particles on a filter and the measurement of the change in transmittance through the filter to obtain absorption as is done by the particle soot absorption photometer (PSAP) and aethalometers (Bond 1999; Weingartner et al. 2003; Sheridan et al. 2005). However, the chemical composition and morphology of the particles can change during deposition onto the filters leading to measured optical properties that may differ from those measured in-situ (Subramanian 2007). Also, these bulk filter methods do not provide single particle measurements. Photoacoustic spectroscopy (Arnott et al. 1999; Arnott et al. 2005; Lack et al. 2006) has demonstrated accurate in-situ absorption measurements. Cavity ringdown spectroscopy (O'Keefe and Deacon 1988) has been employed to provide aerosol extinction measurements with uncertainties of a few percent (Smith and Atkinson 2001; Strawa et al. 2003; Baynard et al. 2007). When combined with scattering measurements such as those from nephelometers, these extinction measurements can be used to extract absorption coefficients as well as provide for the derivation of SSA values. However, due to the importance of factors such as relative humidity on the aerosol optical properties (Baynard et al. 2007) combining measurements from instruments operating under potentially different environmental conditions can lead to uncertainties in the derived optical properties of the aerosols. Strawa and coworkers have developed a bulk measurement instrument that addresses these issues by performing cavity ringdown measurements to obtain the extinction coefficient as well as measuring the scattered light from the same aerosol sample under equivalent conditions eliminating some of the errors described above (Strawa et al. 2003; Strawa et al. 2006).

The Single Particle Soot Photometer (SP2) (Schwarz et al. 2006) instrument performs optical measurements on single aerosol particles. Specifically, SP2 measures the mass of black carbon in single aerosol particles by monitoring the incandescence of the particles after absorption of radiation by the black carbon component. There is a linear relationship between the intensity of incandescence and mass of the light absorbing material. Information about coatings on the particles is also obtained by measurement of scattered light from the particles. The SP2 instrument measures particles with diameters between approximately 90 and 800 nm as compared to the instrument described within this paper that effectively measures particles with diameters in the range of around 300 nm to above a micrometer. The SP2 instrument measures exclusively aerosols containing black carbon and excludes other absorbing aerosols such as mineral dust and those with organic content.

The motivation for the ASTER instrument development described herein is to provide in-situ, single particle measurements simultaneously of extinction and scattering coefficients, providing SSA values for atmospheric aerosols of varying composition. Making both measurements in a single instrument eliminates numerous error sources (i.e., relative humidity differences between instruments). Since it operates in a single particle mode, this instrument is able to determine, for example, if a bulk SSA measurement of 0.9 is due to every particle in the sample having an SSA value of 0.9, 90% particles being pure scatterers and 10% being pure absorbers, or some intermediate mixture. This type of information is lost in bulk measurements that provide single, averaged SSA values. Single particle information will also help track the changes in absorption that occur as light-absorbing particles acquire coatings or are otherwise processed in the atmosphere. The experimental results presented here are preliminary and reflect the intermediate state of development ASTER currently resides in. The errors and uncertainties in these results will be used to make further improvements to the instrument.

INSTRUMENT DESCRIPTION AND PERFORMANCE

Instrument Design

The optical layout of ASTER is shown in Figure 1a. The particle-laser interaction cavity consists of three high reflectivity mirrors (99.99%) in an equilateral triangle configuration. The ring configuration is employed as it produces a traveling cavity wave with three advantages over a standing cavity wave. First, forward and backward scattered light is separable in a traveling wave cavity. The separation of the forward scattered light component is necessary for the optical sizing measurements. Second, light scattering in a standing wave cavity might be inconsistent due to particles encountering nodes or antinodes. Finally, optical feedback into the diode laser is reduced by non-normal incidence on the input cavity mirror surface in a ring cavity. Each leg of the cavity triangle is 22.5 cm, corresponding to a free spectral range (FSR) of 444 MHz. The finesse of the cavity is ~21000 calculated from the expression $\pi R^{0.5}/(1\text{-}R)$ where R is the mirror reflectivity. From the value of the finesse and the FSR, the cavity linewidth is calculated to be 21 kHz. The ringdown time for the empty cavity is 7.5 μs and is measured periodically to determine mirror reflectivity. The Gaussian beam waist at the midpoint of each leg of the triangle is calculated to be 340 μm × 380 μm.

An external-cavity diode laser (New Focus 6000 Vortex series) generates 672 nm light with an output power of 10 mW that is incident on the three-mirror interaction cavity. This laser source was chosen for several reasons. The diode laser provides a compact, rugged laser source that is ideal for eventual field deployment. Also, operation at 672 nm avoids water absorption lines that could affect the extinction measurements. Multiple-wavelength measurements would provide additional, valuable information. In principle, ASTER could be operated at other wavelengths by simply modifying the optics in the measurement cavity. However, due to the nature of the frequency stabilization employed, 672 nm is convenient. There are other potentially usable wavelengths, especially in the infrared (IR). The diode output beam passes through a Faraday isolator for optical feedback suppression, then an anamorphic prism pair to correct the elliptical profile of the diode laser beam. The electro-optical modulator (EOM) frequency modulates the beam at 30 MHz for frequency locking of the diode laser to the interaction cavity as discussed below. The beam then encounters an acousto-optic

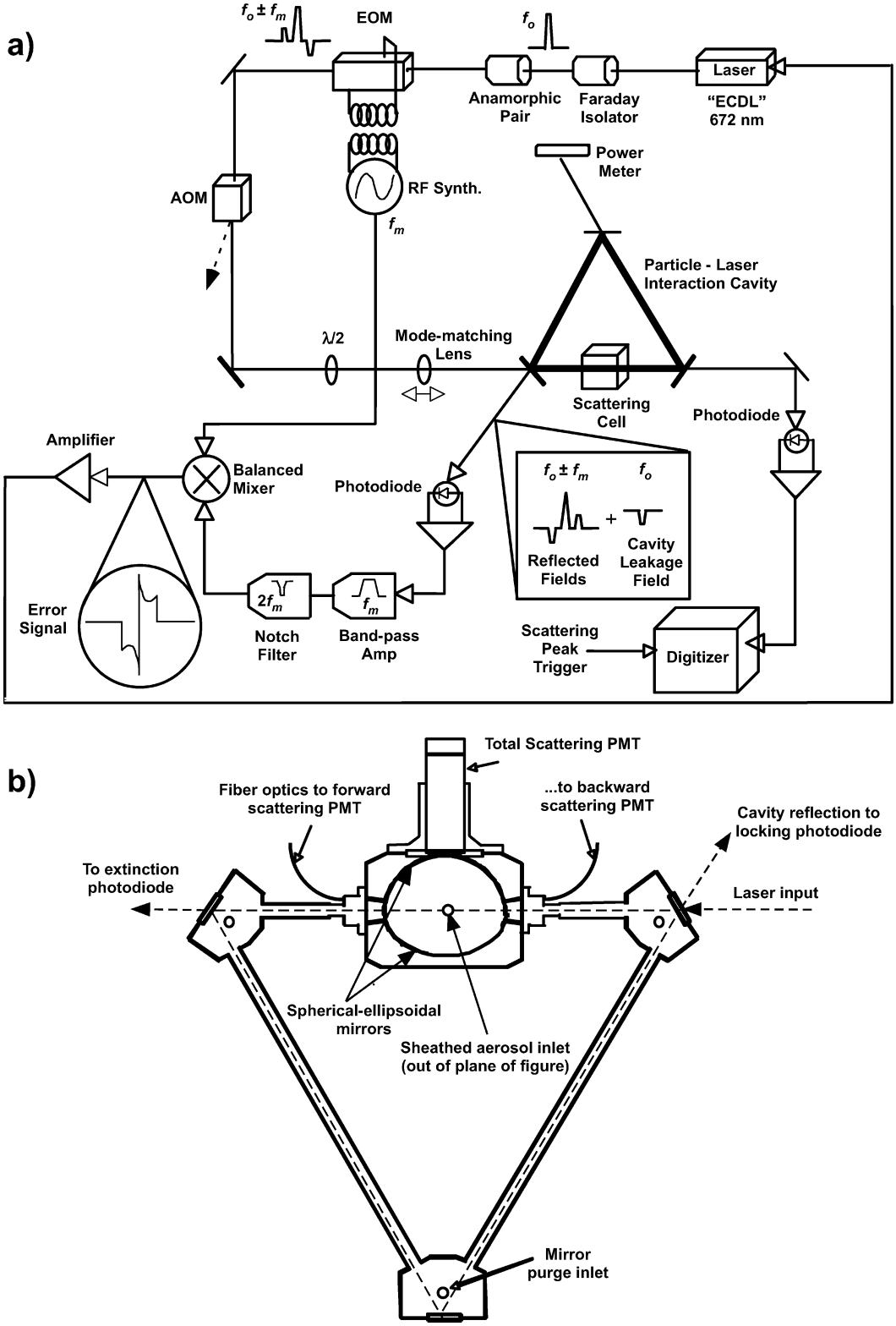

FIG. 1. (a) Instrument optical and locking layout. Optical components are mounted to an optical table that itself is located on a larger optical table with vibrational damping mounts. The entire system can be enclosed to suppress air currents and stray ambient light if desired. (b) Diagram of the scattering cell and mirror enclosures showing a top view of the three-mirror cavity. The scattering cell is rotated 45° out of the plane of the paper in the instrument. The forward and backward scattering ports each contain seven fiber optic cables in a circular pattern about the beam axis. Only one of each is shown. Also, not shown is the aerosol outlet that is out of the plane of the figure on the other side of the aerosol inlet.

modulator (AOM) that diffracts the input beam when a voltage is applied to the modulator crystal. The first-order diffraction is incident on the interaction cavity. The AOM provides a method to extinguish the cavity pump beam and initiate a cavity ringdown event when desired. A λ/2-plate is used to rotate the linearly polarized light 90° to obtain an s-polarized beam as the cavity mirrors have a higher reflectivity and thus a higher finesse with s-polarized light. The final pre-cavity optical component is a lens to provide for spatial mode matching between the input beam and the cavity modes.

To achieve a consistent beam shape in the laser-particle interaction region, we align to the nearly circularly symmetric transverse electro-magnetic ($TEM_{0,0}$) cavity mode. The cavity mode structure is evaluated by monitoring the cavity transmission as the frequency of the diode laser is swept across more than one free spectral range of the cavity. When aligned properly the $TEM_{0,0}$ mode is at least an order of magnitude more intense than the other cavity modes. This allows for single-mode $TEM_{0,0}$ operation and minimizes locking to a higher order mode during data collection.

Frequency Stabilized Laser Locking

The diode laser used as a source is inherently noisy with frequency fluctuations around the central lasing frequency on different timescales. The frequency noise is dominated by jitter on slower timescales due to thermal or mechanical effects. Suppression of these frequency fluctuations relative to the cavity narrows the laser linewidth and leads to a very large power buildup in the cavity scaling as the inverse of the cavity mirror transmission (1/T). Laser sources of modest output power can then be used to achieve high circulating powers in the interaction cavity. To achieve this locking one needs to measure the frequency fluctuations of the diode laser against the cavity and provide feedback to the laser to correct these fluctuations over a bandwidth on the order of 1 MHz.

The diode laser is locked to the particle-laser interaction cavity by the Pound-Drever-Hall (PDH) technique (Drever et al. 1983). The technique is described here in limited detail with more thorough discussions found elsewhere (Fox et al. 2002; Black 2001). The particle-laser interaction cavity is used as the stable frequency reference. Reflected intensity from the input cavity mirror interferes with the transmitted fraction of the cavity wave to provide a measure of the frequency match between the laser and the cavity. When the diode laser is on resonance with a cavity mode the reflected intensity goes to a minimum. Frequency modulation of the input beam followed by phase-sensitive detection of the reflected intensity yields an error signal to correct the laser's fluctuations.

The diode laser output is frequency modulated at 30 MHz by the electro-optical modulator shown in Figure 1a. After modulation by the EOM the laser electric field incident on the cavity can be written as having a component at the central diode laser frequency (f_0) and two sideband components. When f_0 is roughly aligned with a cavity mode the sideband components are outside the resonance and predominately reflected. In addition the field at f_0 reflected from the cavity is attenuated and phase shifted relative to the input beam. When detected by a photodetector, the photocurrent modulation at 30 MHz exhibits a maximum when the laser is tuned to either side of the cavity resonance. The signal is bandpass filtered and combined in a balanced mixer with the local RF oscillator used to drive the modulation in the EOM to produce an error signal, the magnitude and polarity of which depends on the frequency mismatch between the diode laser and the reference cavity. This error signal is then sent to the diode laser via a feedback loop amplifier to suppress the frequency fluctuations and to provide locking to the interaction cavity.

The feedback loop amplifier electronics design is based on that described by Fox and coworkers (Fox et al. 2002). The first stage filters and amplifies the error signal from the mixer. The second op-amp stage provides gain to the high frequency corrections and is connected directly to the laser diode current through a resistor. The second stage output is integrated to provide a signal to the piezoelectric transducer thus varying the output laser frequency over slower timescales. The lock performance was initially optimized by modeling the loop behavior as a function of varying the components in the op-amp stages. The lock has proved to be quite robust in the laboratory setting with continuous single-mode locking on the $TEM_{0,0}$ cavity mode over the course of many hours with no loss of locking or mode hops to other cavity modes. The locking can be monitored by either visual observation of the spatial pattern of the mode on a white card placed just after a cavity mirror or by changes in the DC level of the photodiode signal that measures the light leakage through one of the cavity mirrors. The $TEM_{0,0}$ mode corresponds to the maximum photodiode DC level and any sudden decreases in this level are most likely the result of locking to another cavity mode or the loss of locking altogether. Reacquisition of locking is carried out by manually adjusting the injection current on the diode laser power supply, although occasionally spontaneous relocking does occur soon after laser lock is lost.

Particle Measurements

The scattering cell consists of a spherical/ellipsoidal mirror pair (Figure 1b). The ellipsoidal mirror focuses scattered light from one hemisphere onto the total scattering photomultiplier tube (PMT) located orthogonal to both the beam axis and the particle flow path. Light scattered into the other hemisphere is sent back through the origin by the spherical mirror to the ellipsoid and then to the PMT providing light collection over a nearly 4π solid angle. The spherical/ellipsoidal pair collects light more efficiently if scattered from the center of the region than from areas outside of the center. This property provides a way to discriminate against particles that have either escaped the sheath flow or reside in other areas of the beam path.

Light scattered by the particles in the forward and backward directions with respect to the beam axis are also collected in

independent measurements. In both cases a series of seven 4-mm diameter lenses are arranged in a circular pattern around the center of the beam. These lenses are coupled to fiber optic cables that are bundled and fed to two separate PMTs. Light scattered in these directions is collected at angles between 4.6° and 8.5° from the beam axis on each of the seven lenses. The angle of maximum collection is 6.4° due to the use of circular lenses. The different signal levels in the three scattering channels each require different gains. These gains are provided by separate power supplies for each PMT.

A photodiode resides outside of the interaction cavity behind one of the cavity mirrors (Figure 1a,b). The photodiode measures the small fraction of light in the cavity that is transmitted through one of the cavity mirrors. This photodiode signal is used in aligning and optimizing the frequency-swept cavity modes. It also measures the depletion of the cavity light as single particles traverse the beam in the scattering cell. The measured depletion is the sum of scattering and absorption (extinction) of the cavity light by each particle. The cavity depletions appear as Gaussian-shaped peaks on the dc extinction photodiode signal that are absent with no particles present. A red filter reduces stray ambient light on the detector and the path from the back of the cavity mirror to the photodiode is partially enclosed to minimize interference on the extinction signal from particles found outside of the cavity that randomly cross the beam.

The entire cavity beam path including the cavity mirrors is enclosed. A diaphragm pump pulls the particles through the beam, and keeps the cavity relatively free of particles in other areas outside of the scattering cell that may potentially lead to stray signals on the detectors. Each mirror has a small purge flow of N_2 to avoid the deposition of particles on the mirrors. The purge flow is typically less than 10% of the combined sheath and particle flow and is introduced roughly 5 cm from the entrance to the scattering cell. Also, the distance between the tip of the particle nozzle and the laser beam is only 2 cm. The purge flow should have a negligible effect on the sheath flow. This will be investigated in future flow modeling of the system. Along the beam path is a circular aperture that suppresses modes other than $TEM_{0,0}$.

Particles enter the scattering cell perpendicular to the laser beam located in the center of the cell. As the particles interact with the laser, light is scattered out of the beam and directed towards the three PMTs. Simultaneously, the extinction photodiode measures depletions in the dc voltage signal as particles traverse the beam. The wide-angle scattering signal triggers two National Instruments 5122 two-channel digitizers that acquire signals on the three scattering channels and the extinction channel.

The data acquired for a single, purely scattering polystyrene latex sphere (PSL) with a diameter of 900 nm are shown in Figure 2. The amplitude axes vary for the four channels due to different signal levels and accompanying gain settings for the PMTs and the photodiode. The axes are not quantitatively labeled, but typical measured signal levels for a 900 nm diameter particle are approximately 5 V with a 20 mV peak-to-peak baseline noise for the wide-angle scattering, 1 V with 40 mV peak-to-peak noise for the forward scattering channel, 300 mV with 40–50 mV peak-to-peak noise for the backward scattering channel, and 100–200 mV signals with 10 mV noise for the

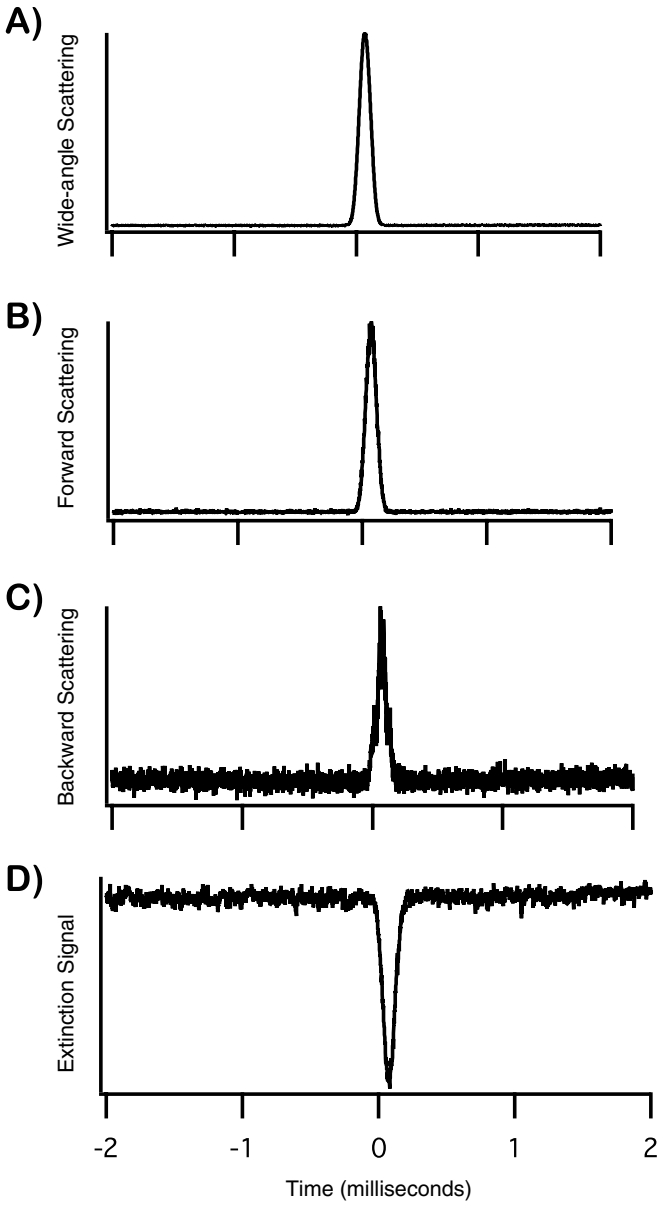

FIG. 2. Photomultiplier and photodiode traces for the four data channels for a single 900 nm PSL particle. A) The wide-angle scattering collected by the spherical/ellipsoidal mirror pair. B) The forward scattering collected by the lens/fiber optic coupled detector. C) The backward scattering collected by the lens/fiber optic coupled detector opposite the forward scattering detector. D) The extinction signal represented by depletion in the cavity light leakage through one of the mirrors and collected by a photodiode. The relative signal strengths are seen by the changes in signal to noise from A) to D). The photomultiplier tube gain voltages and photodiode gain setting are set individually to both maximize signal-to-noise as well as well as to avoid detector saturation.

photodiode extinction channel. These values are dependent on the gain settings on the detectors, as well as particle size and optical properties.

The time axis is the same for all four traces. Time zero represents the point at which the scattering threshold voltage has been achieved rather than when the particle reaches the center of the laser beam. The signals are Gaussian in shape corresponding to traversing through a Gaussian laser intensity profile. The peak widths have a full width half maximum of on the order of 1 μs giving an estimate for the transit time of the particle through the beam. The widths can be adjusted by variation of the particle flow rate.

The differences in the signal-to-noise (S/N) levels between the measurement channels are evident from the traces in Figure 2. The largest signal is the wide-angle scattering (Figure 2a), which is the case for all of the purely scattering PSL data. For the relatively large 900 nm spheres, the forward scattering amplitude (b) is also quite large with favorable S/N. The wide-angle scattering PMT gain voltage is set to avoid detector saturation that occurs with the larger particles. The signal amplitude diminishes considerably with the backward scattering (c) illustrated by the decreased S/N. The extinction measurement (d) also has poorer S/N due in part to measuring a small change in signal against a bright background. The scattering measurements are made against an essentially zero background.

Data Analysis and Filtering

The measured quantities of interest for ASTER are the single-scattering albedo (SSA) and a representation of size of each particle. The SSA is the ratio of scattering to extinction. The scattering for each particle is the sum of the wide-angle scattering, forward scattering, and backward scattering. For the particles below about 500 nm in diameter, the backward scattering is not used due to poor S/N. Backward scattering measurements are omitted from the data presented here. For the sizing of particles, the ratio of the forward scattering to the total scattering (wide-angle + forward) is used as a proxy for particle diameter. Some instruments, such as optical particle counters, measure particle diameter by the amount of scattering over large solid angles. This assumes that all particles travel through the center of the beam encountering the same laser intensity profile, so there is no position dependence to the scattering. The forward to total scattering ratio is more robust in that to a first approximation it is not dependent on particle position in the laser beam.

Sizing by amount of scattering is also dependent on the indices of refraction of the particles. This can lead to uncertainties in the sizing for samples that contain particles with multiple refractive indices. Truncation errors, especially in the forward scattering lobe, also lead to sizing errors. Mie scattering calculations using the ASTER scattering geometry were carried out to study these effects. The calculations were carried out for a series of indices of refraction including partial absorption for one value. The calculated scattering cross section is integrated over the angles 8.5° to 171.5° in each hemisphere representing the ASTER wide-angle collection geometry. The calculated forward scattering is integrated between 4.2° and 8.5° and is weighted to reflect the collection efficiencies of the lenses. The backward scattering geometry in this calculation is symmetric with the forward scattering.

Figure 3a shows calculations for the total collected scattering cross section as a function of particle diameter for various indices of refraction. For particle diameters less than 1 micrometer, the cross sections show a clear dependence on refractive index ranging over an order of magnitude at a given particle diameter. Particle sizing based on the total collected scattering for

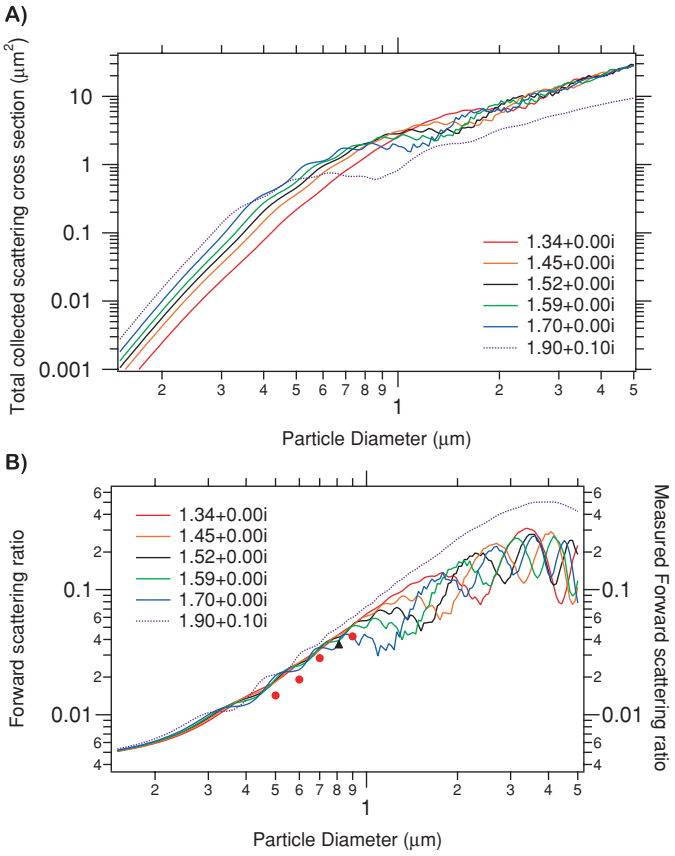

FIG. 3. Mie scattering calculations for a series of indices of refraction for varying spherical particle diameter. (a) Calculated total collected scattering cross section versus particle diameter. Each curve represents calculations carried out at the color-coded index of refraction. The calculated scattering cross section is integrated over the angles 8.5° to 171.5° in each hemisphere representing the ASTER wide-angle collection geometry. (b) Calculated forward to total scattering ratio as a function of particle diameter. The forward scattering ratio is the calculated forward scattering divided by the sum of calculated wide-angle, forward, and backward scattering. Also, shown are mean ASTER measured values of the forward scattering ratio for nominal PSL diameters of 500, 600, 700, 811, and 900 nm. Points in red represent purely-scattering PSLs with an index of refraction of 1.59 + 0.00i. The black triangle represents partially-absorbing spheres with an idex of refraction of 1.775 + 0.04i. The two scattering ratio axes are different due to one being a calculated quantity and the other being a measured quantity that can vary with varying detector gains.

ASTER (and for optical particle counters) is inaccurate for samples with varying indices of refraction. Figure 3b is similar to 3a, but now the ratio of the calculated forward scattering to total collected scattering is shown versus particle diameter. There is very little dependence on index of refraction below diameters of 1 micrometer when the forward scattering ratio is used for sizing. Above 1 micrometer the variation ranges over about a factor of two. Figure 3 clearly depicts the advantage of using the ratio of forward scattering to total scattering as method of sizing particles in ASTER by removing most of the dependence on refractive index for submicron particles. It also largely removes the spatial dependence of the particle in the beam as well as any laser intensity fluctuations.

The measured quantities used to calculate the SSA and scattering ratios are obtained by fitting Gaussian lineshapes to the scattering and extinction signal traces. The LabVIEW-based analysis program returns the following for each data channel: peak amplitude, peak width, peak position, chi-squared value, and area of the Gaussian peak fits. The SSA and scattering ratios were calculated using both peak amplitude and peak area of the Gaussian fits for comparison. There were no discernible differences between the two and all results presented here are based on the peak heights of the Gaussian fits. Another instrument that measures particle scattering digitally integrates the scattering amplitudes to minimize the effects of signal noise (Dick et al. 2007). Directly integrating the peaks without the Gaussian fits in ASTER will be explored to determine if this improves the quality of the data. The Gaussian fit parameters would still be needed for data filtering.

The particle data are filtered based on the Gaussian fit parameters. Any data files with zero or negative values for peak amplitudes or peak widths on any of the four channels are filtered out. The fitting program occasionally returns negative or zero values when it attempts to fit a non-Gaussian-like signal such as transient, large amplitude noise on the photodiode and PMT channels. Poor fits are usually due to peaks with very small S/N, but may also be due to more than one particle in the beam. Fits with large peak widths are also discarded as these are most likely caused by particles exiting the sheath and taking a nonlinear path through the beam leading to a longer residence time. Flow modeling was not carried out for this version of ASTER, however this will be undertaken in the future for the modified version of the instrument. Roughly 10–20% of the data were filtered out for the results presented here.

Laboratory Results and Discussion

The instrument performance in its current state of development was assessed by measurements on purely scattering and partially absorbing polystyrene latex spheres of known diameters. SSA and scattering ratios were obtained for laboratory-generated particles with diameters that range from 500 to 900 nm corresponding to size parameters of 2.34 to 4.21. The size parameter is the ratio of the particle diameter to the wavelength of incident light multiplied by a factor of π. Particles with these size parameters undergo scattering that resides in the Mie scattering regime (Van de Hulst 1981).

Polystyrene latex spheres (Duke Scientific) of various diameters were used as pure scatterers (SSA = 1) with no absorption at 672 nm. A few drops of the polystyrene spheres (PSL) solution with a chosen mean diameter were diluted in 50 mL of distilled water and nebulized with a Collison Nebulizer (BGI, Incorporated). The particles were passed through a drying volume and enter a Differential Mobility Analyzer (DMA) for size selection. The flows and column voltages are calibrated with an Ultra High Sensitivity Aerosol Spectrometer (UHSAS) from Droplet Measurement Technologies and a TSI Condensation Particle Counter. These calibrations are carried out for each sample with a given mean particle diameter to maximize the transmission of particles with that diameter through the DMA. The relative humidity of the DMA output was about 20% for the data presented here.

The DMA-selected particles were introduced into the center of the scattering cell roughly 2 cm from the laser beam waist using a customized nozzle (Droplet Measurement Technologies) that includes a sheath flow of filtered N_2. The position of the combined nozzle-scattering cell assembly may be adjusted independently of the laser beam position allowing for variation of the overlap of particles and laser beam. The overlap is optimized by monitoring the peak amplitudes of the forward and wide-angle scattering channels. The largest signals on these two channels occur when the particles pass through the center of the laser beam. The small laser interaction volume dictated by the geometry of the cavity and low ambient particle concentrations in clean conditions lead to low probability of multiple particles being in the beam at once. Laboratory particle samples were diluted to achieve this condition.

The experimentally derived SSA and forward-to-total scattering ratios are shown in Figure 4. The data are color coded by the manufacturer-specified mean diameter of the PSL sample used to prepare each particle mixture. The mixtures were then further size-selected using the DMA. For these data, the backward scattering quantity is not used in deriving the SSA values and the scattering ratios. Thus, the total scattering is the sum of forward and wide-angle scattering. The total scattering is divided by the extinction amplitude to yield an unscaled value of the SSA. This experimentally measured ratio must be scaled to account for the differing gains of the scattering PMTs and extinction photodiode as well as imperfect collection of the scattered light. These gains are scaled to set the average SSA obtained from the purely scattering PSL to one. Note that there are two free parameters (the gains of the wide-angle and forward channels relative to extinction) for the five particle sizes presented in Figure 4. Performing measurements on multiple particle sizes yields more than one independent measurement allowing for the two free parameters to be determined from only one constraint (SSA).

Measurements were also made on partially-absorbing spheres to determine if changes in SSA are measurable with ASTER. In

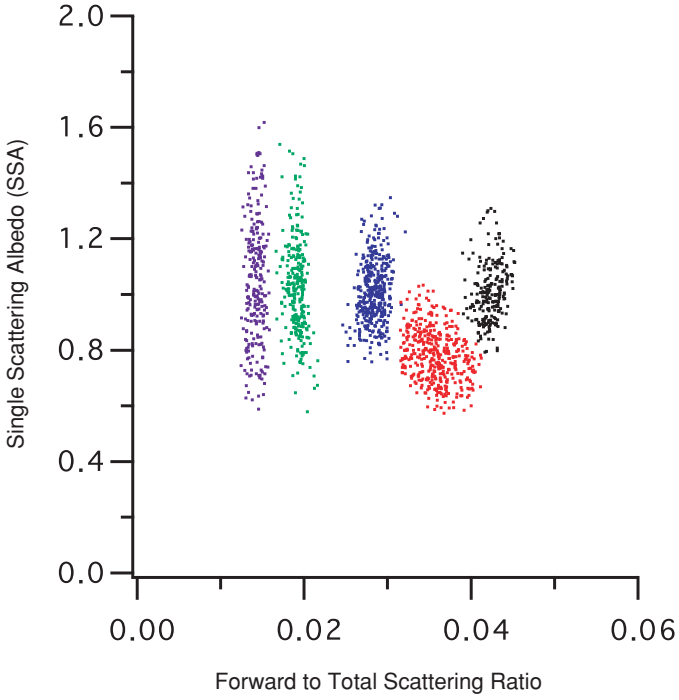

FIG. 4. Measured single-scattering albedo (SSA) versus forward to total scattering ratio for DMA size-selected polystyrene latex spheres (PSL). The SSA values are determined from the ratio of measured total scattering amplitude (sum of wide-angle scattering amplitude and forward scattering amplitude) to the measured extinction amplitude for each particle. The forward to total scattering ratios for each particle are used as a proxy measurement for particle diameter. The particle data points are color coded by the mean diameter of the PSL mixture used to generate the particles that were then selected by the DMA. Points in purple represent a nominal particle diameter of 500 nm, green for 600 nm, blue for 700 nm, red for absorbing 811 nm, and black represents 900 nm particle diameters. The PSL samples that are pure scatterers have albedos scaled to 1. This scaling is used to determine the SSA values of the partially-absorbing spheres with a mean diameter of 811 nm. The mean SSA after scaling against the pure scatterers is 0.79, which is in agreement with a photoacoustic measurement of 0.77 made on the same partially absorbing particles. All data points were acquired on the same day with only the particle generator sample and DMA voltages changed. All other conditions are held constant.

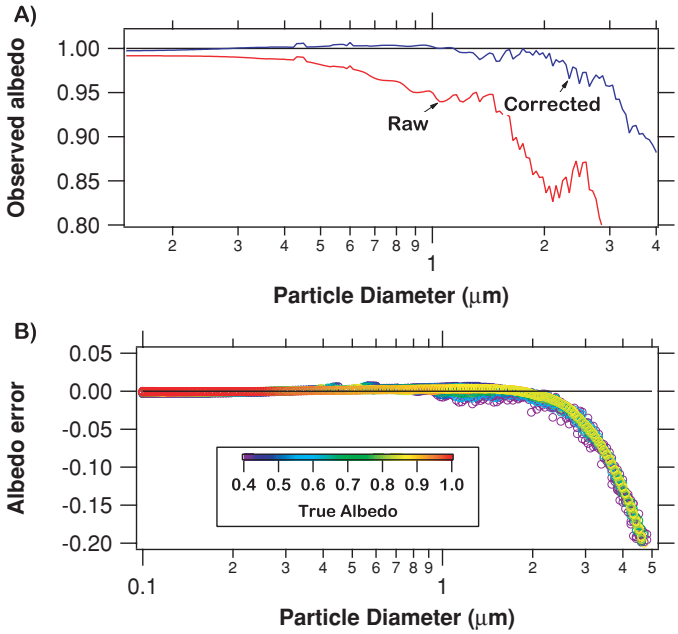

FIG. 5. Calculations of the effect of truncation errors on ASTER. (a) Observed albedo is the calculated albedo that is measured by ASTER taking into account the collection geometries with the associated trucation of forward and backward scattered light. This case is labeled "raw." The corrected trace has the calculated forward scattering multiplied by a factor of 2.09 to account for the forward light truncation. (b) Albedo error as a function of particle diameter where albedo error is the corrected observed albedo plotted in (a) minus the true albedo. True albedo is the calculated albedo assuming perfect scattered light collection (i.e., no forward or backward truncation). The curves are color-coded by true albedo, essentially showing the albedo error dependence on index of refraction.

this case, dyed PSL with a measured average diameter of 811 nm (Lack et al. 2006) were generated and DMA size-selected by the method described for the purely scattering spheres. The data for the absorbing spheres are shown in Figure 4 depicted by the red dots. The absorbing spheres have forward scattering ratios that place it between the ratio values of the 900 nm and 700 nm spheres. Using the scaling from the purely scattering, calibration spheres, these dyed spheres have a scaled average SSA of 0.79 indicating partial absorption. This value is in agreement with that measured in a photoacoustic spectrometer of 0.77 for particles taken from the same batch (Lack et al. 2006).

Mie scattering calculations are again employed to investigate the dependence of the ASTER SSA measurements on particle optical properties and diameters. Figure 5 shows the calculated SSA as a function of particle diameter. The red trace labeled "raw" in Figure 5a represents calculations of the observed SSA taking into account the truncation in the ASTER collection geometry. The calculations use an index of refraction of 1.59, that of PSL spheres, and represent SSA values of 1.0. The deviation from SSA = 1.0 is present for all particle diameters and increases with increasing diameter. The blue trace labeled "corrected" is the same calculation, but now contains a factor of 2.09 that the forward scattering is multiplied by to correct for the truncation errors in the ASTER geometry. The observed SSA is now very close to the correct value of 1.0 for particle diameters up to 2.0 μm.

Figure 5b essentially expands Figure 5a now allowing the SSA to vary for the particles. The albedo error is the difference of the calculated ASTER-measured SSA with the 2.09 correction factor from the expected SSA of the particle with a perfect collection geometry. The difference between the measured and the true SSA is very small out to diameters of 2.0 μm, even for particles with very low SSA values. These calculations show that ASTER should be able to produce accurate SSA over a range of particle scattering and absorption when the forward truncation is properly accounted for.

Based on Mie calculations, Figure 3 shows that the forward scattering ratio provides a proxy measurement of particle

diameter that monotonically increases with diameter and is independent of particle refractive index for particles up to 1.0 μm. The means of the forward scattering ratio for each particle size group in Figure 4 are shown as individual points in Figure 3b. The red points are the purely scattering spheres and the black triangle is the mean for the partially absorbing spheres. The two y-axes are different, because one is a calculated value and the other is the instrument-measured value. However, the measured values are qualitatively consistent with the calculated values and do not show any dependence on refractive index. This indicates ASTER provides a consistent measure of particle size in the submicrometer range after calibration with known particle diameters.

Measurements were also made on ambient, laboratory air to determine the performance on an unknown sample that would be encountered in a field setting. The data for these ambient particles are shown in Figure 6 and are presented as scaled SSA versus forward scattering ratio as in Figure 4. The SSA values were scaled using calibration data from purely scattering PSLs with diameters of 240, 600, and 800 nm. Overlaid in the graph is the histogram of the scaled SSA values. Inspection of both the SSA versus forward scattering ratio and the histogram show the majority of ambient particles with SSA values near 1.0 (purely scattering) and a small mode of particles centered near an SSA value of 0.4, indicating appreciable absorption. The calibration data is also used to determine the relationship between particle diameter and forward scattering ratio. The size distribution peaks at forward scattering ratios below 0.1 with the maximum in the distribution near 0.07. The maximum of the ambient particle scattering distribution at 0.07 then corresponds to a particle diameter of around 300 nm with the distribution extending to diameters just above a micrometer. There is a sharp drop in data points below the maximum in the size distribution reflecting the current small size limit of ASTER. Also, there are not many particles with diameters above a micrometer most likely due to the PMT saturation issues and subsequent filtering out of very large particles.

It is likely that the ambient data no longer contain particles that are only spherical in shape. For non-spherical particles, the use of the forward to total scattering ratio as an indicator of size may no longer be valid. To investigate this effect, the peak shapes for the ambient particles were visually inspected for deviations from a Gaussian lineshape and for poor fits. A large majority of the ambient particles retain the Gaussian shape that is observed for the laboratory-generated spherical PSL particles. A small fraction of the particles that are retained after data filtering possess scattering and extinction peaks that show slight deviations from the Gaussian of the spherical particles. These deviations are generally in the form of slightly asymmetric peaks or modulations on the otherwise Gaussian lineshapes. The observed deviations from Gaussian shapes in this data set occur for larger particles. However, it is difficult to observe deviations for the smaller particles with lower S/N. Small diameter, non-spherical particles may be present, but currently are not discernible.

The ambient data was also color-coded by chi-squared values for each of the three data channels, though not shown here. The outlying chi-squared values were almost exclusively for particles with the smallest forward-to-total scattering ratios near or at the measurement cutoff. Those particles though to be non-spherical did not have chi-squared values dissimilar from those with Gaussian lineshapes. Poor fits appear to be predominately a function of low S/N for the smallest particle diameters measured.

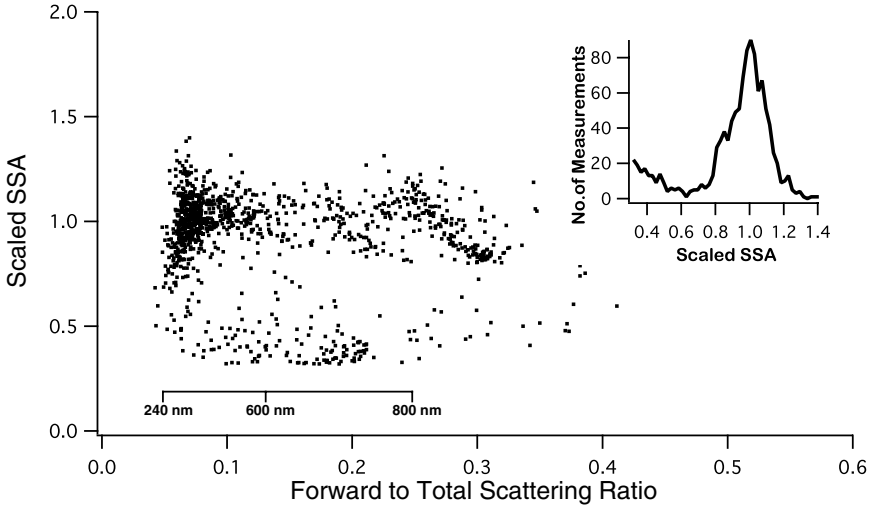

FIG. 6. Single-scattering albedo (SSA) and scattering ratio measurements for ambient particles in the laboratory. The ambient SSA values are scaled using laboratory-generated particles with SSA = 1. Three different PSL diameters are used to determine the size scaling for the forward to total scattering ratios for these ambient particles. The top axis shows the nominal PSL diameters used to calibrate particle diameter to scattering ratio. Inlaid on the plot is a histogram of the SSA data. The dominant peak is at SSA = 1 with a smaller mode below 0.5. Based on the calibration data of particles with known diameters, the large concentration of particles just below a scattering ratio of 0.1 have diameters of approximately 300 nm.

A future study will involve measuring particles known to be nonspherical to determine the shapes of the signal traces and quality of Gaussian fits in a more controlled experiment.

Measurement Uncertainties

Figure 4 provides information on the magnitude of uncertainties associated with the SSA and forward scattering ratio measurements for ASTER in its current development state. In Figure 4, four groups of particles are chosen with SSA = 1: they scatter all of the radiation impinging on them with no absorption. The spread in the scaled SSA values increases with decreasing forward scattering ratio, with roughly half of the values for a given particle diameter greater than 1. The standard deviations from the scaled mean SSA values of 1 for each group of particles are 0.105, 0.090, 0.116, 0.174, and 0.216 for 900 nm, 811 nm, 700 nm, 600 nm, and 500 nm, respectively. This indicates the increasing uncertainty with decreasing particle diameter for the SSA measurements. The mean scattering ratios and standard deviations for decreasing nominal particle diameter are 0.0423 ± 0.0013, 0.0358 ± 0.0023, 0.0284 ± 0.0012, 0.0191 ± 0.0008, and 0.0142 ± 0.0007. The spread in the scattering ratios follows roughly the opposite trend of the SSA with generally decreasing spread in the values with decreasing particle diameter.

The sheath-to-particle flow ratios were varied from just above 10:1 down to about 1:1 with no drastic changes in the mean values of the forward scattering ratios and the SSA values. There were slight differences in the shapes and widths of the histograms with the various flow ratios. Likewise, changing the overall flows in the instrument over roughly a factor of two at the same sheath to particle flow ratios yielded no major changes in the scattering ratios and SSA values, but there were some changes in the standard deviations of these values with the changing flows.

During measurements, the intensity of the cavity laser beam drifts while remaining locked to the $TEM_{0,0}$ mode. This drift is observable on either the dc level of the extinction photodiode or by measuring the laser power transmitted through one of the cavity mirrors. The drift is corrected for by adjustment of the cavity mirrors or the injection current into the diode laser. The laser intensity in the cavity was systematically varied to determine the effect of changing intensity on the SSA and particle size measurements. The SSA and scattering ratios for size-selected 600 nm particles were acquired at four different $TEM_{0,0}$ intensity levels spanning about a factor of two in intensity. Histograms of the data show a drift of 5% in the mean SSA values between the high and low intensity levels with a narrowing of the distribution for the lower intensities. The scattering ratios show an 8% change between the two intensity extremes with a somewhat smaller change in distribution width. These drifts reflect changing alignment of the system with time and are not sufficiently corrected for by the Pound-Drever-Hall locking scheme. These drifts add a few percent of uncertainty in the measurements if not monitored and corrected for.

The quality of the Gaussian fits to the measured scattering and extinction peaks are an indicator of sources of measurement uncertainty. The data processing program returns a chi-squared value of the Gaussian fit that is used as a measure of the fit quality. A lower chi-squared value represents a better fit to the measured scattering and extinction peaks. For the 900 nm particles in Figure 3, the mean chi-squared values for the wide-angle scattering, forward scattering, and extinction fits are 2.5×10^{-5}, 4.6×10^{-4}, and 3.2×10^{-3}, respectively. This implies that as the S/N decreases the Gaussian fits to the data become poorer. Also, comparing the mean chi-squared values of the extinction fits for each particle size group yields 3.2×10^{-3} for 900 nm, 3.5×10^{-3} for 811 nm, 1.3×10^{-2} for 700 nm, 3.3×10^{-2} for 600 nm, and 5×10^{-2} for 500 nm. An error propagation calculation is not performed here, but the primary source of error in the SSA values most likely resides in the extinction amplitude channel as eluded to by the chi-squared values. It has the poorest S/N of the other channels used here and in turn the poorest Gaussian fits. With the laser locked to the $TEM_{0,0}$ and instrument flows present, the noise on the extinction photodiode is at least an order of magnitude greater than the shot-noise limit of the photodiode detector. Suppression of this additional noise should improve the S/N on the extinction signals and thus the Gaussian fit leading to better quality SSA data.

The effective diameter range over which reliable measurements can be made is determined by the S/N on the small diameter end and by saturation of the detectors on the large diameter range. The Mie calculations displayed in Figures 3 and 5 also show a breakdown in SSA and forward ratio measurements for particles with diameters above about 2 μm. This also caps the diameter range if one wishes to perform measurements on particles with varying index of refraction. The arguments above on the increasing uncertainty in SSA measurements put a lower limit on the particle diameter. For the data depicted in Figure 4, changes in SSA less than 50% are probably not detectable below 500 nm due to increasing uncertainty in the extinction measurements. However, for the ambient particles in Figure 6 the spread in SSA values is smaller down to around 300 nm than previously measured in Figure 4. These two sets of data were taken a few months apart with the ambient data taken just after an optics cleaning. This cleaning leads to increased mirror reflectivity and thus a higher cavity finesse. This higher finesse in turn increases the extinction.

In this study, data for particles above 900 nm were not reported for two reasons. The first is that particles much larger than this produce saturation on the wide-angle and forward scattering detectors. A solution yet to be implemented in this instrument builds on the work of Gao and coworkers where Gaussian fits are only carried out on the leading edge of a peak to provide a fit for the entire peak (Gao et al. 2007). This would allow for data from saturated peaks associated with large particles to be retained. The second reason for the avoidance of particles above 900 nm is due to limitations in the DMA.

SUMMARY AND FUTURE WORK

The ASTER instrument is being developed to simultaneously measure scattering and extinction by single aerosol particles from which single-scattering albedo (SSA) and a measure of particle size are obtained. Performing the scattering and extinction measurements in one instrument may reduce uncertainties in SSA values over those arrived at by combining measurements from multiple instruments. Also, single particle data provide additional insights and information to augment bulk SSA measurements. Mie scattering calculations on the ASTER system indicate that particle sizing using forward to total scattering ratios is largely independent of particle index of refraction; a problem that arises in particle sizing instruments, such as optical particle counters. The preliminary results presented here will be used to improve the future performance of the instrument.

A series of size-selected polystyrene latex spheres (PSL) with SSA = 1 were used to calibrate the instrument and assess its performance and limitations. Individual particle size distributions with mean particle diameters roughly 100 nm in separation were clearly resolvable using the forward scattering ratio measurement. The measured SSA values, which should be single-valued, showed a rather large spread in values that increases with decreasing particle diameter. A sample of absorbing, dyed PSL with SSA less than 1 was measured and compared to the calibration particles. Previous measurements on these absorbing particles with other instruments yielded a mean particle diameter of 811 nm and a mean SSA of 0.77. Despite the current resolution of the measured SSA values, the measured ASTER mean value of 0.79 is consistent with that measured by a photoacoustic spectrometer. ASTER was also able to identify a small mode of highly absorbing particles in an ambient air sample.

The data presented here were used to investigate the sources of uncertainty in measurements and limits in the particle sizes over which measurements can be made. These uncertainty and error sources will be addressed in the redesign of the instrument for field deployment. The data show that the spread, and hence uncertainty, in the SSA measurements increases with decreasing particle size due to decreasing S/N in the measured scattering and extinction signals. The low S/N makes reliable SSA and scattering ratio measurements for particles with diameters below 300 nm unlikely for the instrument in its current configuration. It appears that the initial uncertainty sources to be addressed are the low S/N on the extinction channel and also errors in the Gaussian fits to the data.

The first instrument modification to address these issues is to increase the reflectivity of the cavity mirrors. The scattering signals would be larger because of increased circulating laser power inside the cavity. More importantly, the increased mirror reflectivity increases the finesse of the cavity, which would increase the depletion signals leading to improved S/N on the extinction measurements. The noise on the extinction photodiode also increases with flow-induced turbulence that will have to minimized. The interaction cavity in the field instrument will be hermetically sealed to minimize light pollution and keep stray particles out of the laser beam. The enclosure will also reduce stray flows in the system that likely increase noise on the extinction channel. Finally, variations in settings of the frequency locking electronics lead to variations in the amount of noise on the extinction signal. A re-optimization of the locking system must to be carried out to ensure the intensity and frequency fluctuations in the cavity laser beam are minimized.

The collection of the forward and backward scattered light is being modified to decrease the amount of light that is truncated leading to increased signals. This will especially be important for the backward scattered light that currently suffers from very poor S/N due to the small amount of backward scattered light available for measurement. The manner in which the Gaussian fits are performed and signal amplitudes extracted will also be studied in further detail as variation in the fit quality between similar particles undoubtedly leads to spread in the data. Finally, instrument environmental data, such as temperature, pressure, and relative humidity will be recorded as an additional monitor of various effects on the data quality.

REFERENCES

Ackerman, T. P., and Toon, O. B. (1981). Absorption of Visible Radiation in Atmosphere Containing Mixtures of Absorbing and Nonabsorbing Particles, *Appl. Opt.* 20:3661–3668.

Andreae, M. O., and Gelencser, A. (2006). Black Carbon or Brown Carbon? The Nature of Light-Absorbing Carbonaceous Aerosols, *Atmos. Chem. Phys. Discuss.* 6:3419–3463.

Arnott, W. P., Moosmuller, H., Rogers, C. F., Jin T. F., and Bruch, R. (1999). Photoacoustic Spectrometer for Measuring Light Absorption by Aerosol: Instrument Description, *Atmos. Environ.* 33:2845–2852.

Arnott, W. P., Moosmuller, H., Sheridan, P. J., Ogren, J. A., Raspet, R., Slaton, W. V., Hand, J. L., Kreidenweis, S. M., and Collett Jr., J. L. (2003). Photoacoustic and Filter-Based Ambient Aerosol Light Absorption Measurements: Instrument Comparisons and the Role of Relative Humidity, *J. Geophys. Res.* 108:D1. doi:10.1029/2002JD002165.

Black, E. D. (2001). An Introduction to Pound-Drever-Hall Laser Frequency stabilization, *Amer. J. Phys.* 69:79–87.

Bond, T. C., Anderson, T. L., and Campbell D. (1999). Calibration and Intercomparison of Filter-Based Measurements of Visible Light Absorption by Aerosols, *Aerosol Sci. Technol.* 30:582–600.

Bond, T. C., Streets, D. G., Yarber, K. F., Nelson, S. M., Woo, J.-H., and Klimont, Z. (2004). A Technology-Based Global Inventory of Black and Organic Carbon Emissions from Combustion, *J. Geophys. Res.* 109:D14203. doi:10.1029/2003JD003697.

Bond, T. C., and Bergstrom, R. W. (2005). Light Absorption by Carbonaceous Particles: An Investigative Review, *Aerosol Sci. Technol.* 39:1–41.

Bond, T. C., Habib, G., and Bergstrom, R. W. (2006). Limitations in the Enhancement of Visible Light Absorption Due to Mixing State, *J. Geophys. Res.* 111:D20211. doi:10.1029/2006JD007315.

Bond, T. C., Bhardwaj, E., Dong, R., Jogani, R., Jung, S., Roden, C., Streets, D. G., and Trautman, N. M. (2007). Historical Emissions of Black and Organic Carbon Aerosol from Energy-Related Combustion, 1850–2000, *Global Biogeochem. Cycles*. 21:GB2018. doi:10.1029/2006GB002840.

Buseck, P. R., and Posfai, M. (1999). Airborne Minerals and Related Aerosol Particles: Effects on Climate and the Environment, *Proc. Natl. Acad. Sci.* 92:3372–3379.

Chung, S. H., and Seinfeld, J. H. (2002). Global Distribution and Climate Forcing of Carbonaceous Aerosols, *J. Geophys. Res.* 107, D19. doi:10.1029/2001JD001397.

Chylek, P., and Coakley, J. A. (1974). Aerosols and Climate, *Science*. 183:75–77.

Dick, W. D., Ziemann, P. J., and McMurry, P. H. (2007). Multiangle Light-Scattering Measurements of Refractive Index of Submicron Atmospheric Particles, *Aerosol Sci. Technol*. 41:549–569.

Drever, R. W. P., Hall, J. L., Kowalski, F. V., Hough, J., Ford, G. M., Munley, A. J., and Ward, H. (1983). Laser Phase and Frequency Stabilization Using an Optical Resonator, *Appl. Phys. B*. 31:97–105.

Fox, R. W., Oates, C. W., and Hollberg, L. W. (2002). Stabilizing Diode Lasers to High Finesse Cavities, *Experimental Methods in Physical Sciences vol. 40*, Elsevier Science, New York.

Fuller, K. A., Malm, W. C., and Kreidenweis, S. M. (1999). Effects of Mixing on Extinction by Carbonaceous Particles, *J. Geophys. Res.* 104:D13. doi:10.1029/1999JD100091.

Gao, R. S., Schwarz, J. P., Kelly, K. K., Fahey, D. W., Watts, L. A., Thompson, T. L., Spackman, J. R., Slowik, J. G., Cross, E. S., Han, J. -H., Davidovits, P., Onasch, T. B., and Worsnop, D. R. (2007). A Novel Method for Estimating Light-Scattering Properties of Soot Aerosols Using a Modified Single-Particle Soot Photometer, *Aerosol Sci. Technol*. 41:125–135.

IPCC. (2007). *Climate Change 2007: The Physical Science Basis. Contribution of Working Group I to the Fourth Assessment Report of the Intergovernmental Panel on Climate Change*, S. Solomon et.al., ed., Cambridge University Press, Cambridge, United Kingdom, and New York, USA.

Ito, A., and Penner, J. E. (2005). Historical Emissions of Carbonaceous Aerosols from Biomass and Fossil Fuel Burning for the Period 1870–2000, *Global Biogeochem. Cycles*. 19:GB2028. doi:10.1029/2004GB002374.

Jacobson, M. Z. (2001). Strong Radiative Heating Due to the Mixing State of Black Carbon in Atmospheric Aerosols, *Nature*. 409:695–697.

Jacobson, M. Z. (2002). Control of Fossil-Fuel Particulate Black Carbon and Organic Matter, Possibly the Most Effective Method of Slowing Global Warming, *J. Geophys. Res.* 107:D19. doi:10.1029/2001JD001376.

Lack, D. A., Lovejoy, E. R., Baynard, T., Pettersson, A., and Ravishankara, A. R. (2006). Aerosol Absorption Measurement using Photoacoustic Spectroscopy: Sensitivity, Calibration, and Uncertainty Developments, *Aerosol Sci. Technol*. 40:697–708.

Lafon, S., Sokolik, I. N., Rajot, J. L., Caquineau, S., and Gaudichet, A. (2006). Characterization of Iron Oxides in Mineral Dust Aerosols: Implications for Light Absorption, *J. Geophys. Res.* 111:D21207. doi:10.1029/2005JD007016.

O'Keefe, A., and Deacon, D. A. G. (1988). Cavity Ring-Down Optical Spectrometer for Absorption Measurements Using Pulsed Laser Sources, *Rev. Sci. Ins*. 59:2544–2551.

Penner, J. E., Hegg, D., and Leaitch, R. (2001). Unraveling the Role of Aerosols in Climate Change, *Environ. Sci. Technol*. 35:332A–340A.

Posfai, M., Anderson, J. R., Buseck, P. R., and Sievering, H. (1999). Soot and Sulfate Aerosol Particles in the Remote Marine Troposphere, *J. Geophys. Res*. 104:D17. doi:10.1029/1999JD900208.

Schwarz, J. P., et al. (2006). Single-Particle Measurements of Midlatitude Black Carbon and Light-Scattering Aerosols from the Boundary Layer to the Lower Stratosphere, *J. Geophys. Res*. 111:D16207). doi:10.1029/2006JD007076.

Sheridan, P. J., et al. (2005). The Reno Aerosol Optics Study: An Evaluation of Aerosol Absorption Measurement Methods, *Aerosol Sci. Technol*. 39:1–16.

Smith, J. D., and Atkinson, D. B. (2001). A Portable Pulsed Cavity Ring-Down Transmissometer for Measurement of the Optical Extinction of the Atmospheric Aerosol, *Analyst*. 126:1216–1220.

Strawa, A. W., Castaneda, R., Owano, T., Baer, D. S., and Paldus, B. A. (2003). The Measurement of Aerosol Optical Properties Using Continuous Wave Cavity Ring-Down Techniques, *J. Atmos. Oceanic Technol*. 20:454–465.

Strawa, A. W., et al. (2006). Comparison of in situ Aerosol Extinction and Scattering Coefficient Measurements Made During the Aerosol Intensive Operating Period, *J. Geophys. Res*. 111:D05S03. doi:10.1029/2005JD006056.

Subramanian, R., Roden, C. A., Boparai, P., and Bond, T. C. (2007). Yellow Beads and Missing Particles: Trouble Ahead for Filter-Based Absorption Measurements, *Aerosol Sci. Technol*. 41:630–637.

Van de Hulst, H. C. (1981). *Light Scattering by Small Particles*. Dover Publications, Inc. New York.

Weingartner, E., Saathoff, H., Schnaiter, M., Streit, N., Bitnar, B., and Baltensperger, U. (2005). Absorption of Light by Soot Particles: Determination of the Absorption Coefficient by means of Aethalometers, *J. Aerosol Sci*. 34:1455–1463.